Journal of Materials Chemistry A

PAPER

View Article Online
View Journal | View Issue

Cite this: J. Mater. Chem. A, 2014, 2, 9345

Study on SnO_2/graphene composites with superior electrochemical performance for lithium-ion batteries†

Binbin Chen,‡[a] Hang Qian,‡[a] Jianhui Xu,[a] Linlin Qin,[a] Qi-Hui Wu,[b] Mingsen Zheng*[a] and Quanfeng Dong*[a]

Received 28th March 2014
Accepted 22nd April 2014

DOI: 10.1039/c4ta01493f

www.rsc.org/MaterialsA

In this study, the *in situ* growth of tin dioxide (SnO_2) nanoparticles on reduced graphene oxide (rGO) has been realized using a hydrothermal method. The size of the SnO_2 nanoparticles in the SnO_2/rGO composites prepared by three different procedures is about 5 nm, and they are well dispersed on rGO. When applied as anode materials for lithium-ion batteries, we found that the composites synthesized from the stannous oxalate precursor showed the best rate performance and highest cyclic stability. The surface status of the composites, including interactions between SnO_2 and rGO and surface chemical components, was investigated in detail in order to understand why the composites prepared using different procedures displayed vastly different electrochemical performances. The results presented here describe a new approach for the synthesis of uniform and nanosized metal-oxide/rGO composites with excellent electrochemical performance.

1. Introduction

Lithium-ion batteries (LIBs) have attracted considerable research activities owing to their high energy density, high stability and low cost for portable electronics, electric vehicles (EVs) and hybrid electric vehicles (HEVs).[1–3] Graphite is the earliest commercial anode material for LIBs with a limited theoretical capacity of 372 mA h g^{-1},[4,5] which falls behind with the demands of consumers. Since Fuji announced the commercialization of a new LIBs technology using amorphous tin oxide as a negative electrode,[6] tin dioxide (SnO_2) has been the most studied anode material due to its high specific capacity (1494 mA h g^{-1}),[7,8] low cost, abundance and environmental benignity. However, SnO_2 anodes suffer from severe volume change (>300%),[9,10] poor electronic conductivity and the aggregation of Sn clusters during cycling. These shortcomings result in rapid capacity fading and poor rate capability. Generally, two strategies have been explored to alleviate the aforementioned problems. First, the design and fabrication of metal oxide materials with various morphologies and structures on the nanoscale.[11–16] The use of nanostructured electrode materials greatly increases the contact area of electrolyte and active materials, and shortens the lithium ions diffusion paths. Thus, the kinetics of the electrodes is enhanced. Second, metal oxides are combined with conductive matrices such as hard carbon,[17–19] carbon nanotubes,[20–23] and graphene[24–28] to form nanocomposites. Besides the increased conductivity, the combination of conductive matrices can greatly suppress the pulverization and aggregation of nanoparticles during charge–discharge cycles, which is beneficial for the cycle life of electrodes.

Graphene oxide (GO) and rGO have attracted considerable attention in applications involving energy storage due to their two-dimensional open structure and excellent physical and chemical properties.[29–33] Numerous metal oxide/rGO (GO) nanocomposites have been reported as anode materials for LIBs.[34–38] The GO or rGO based nanocomposites showed enhanced cyclic stability and decent rate capabilities as expected. For instance, Zhou *et al.*[39] reported graphene enwrapped SnO_2 hollow nanospheres with improved cycling performance (*ca.* 696 mA h g^{-1} under 0.5 A g^{-1} after 300 cycles) and high-rate capability (*ca.* 307 mA h g^{-1} under 5 A g^{-1}). Nevertheless, in addition to the above-mentioned merits of combining the graphene matrix and nanosized material, the status and interface regarding metal oxides and graphene in the composites are rarely reported. Sun *et al.*[40] demonstrated the existence of chemical bonding between SnO_2 and carbon element by the XANES technique. Similar phenomena were also observed by the Guo group.[41] These findings present a new perspective on the evaluation of metal oxides/rGO composites with superior electrochemical performances. The corresponding design and synthesis of oxides/rGO composites with carefully chosen

[a]State Key Lab of Physical Chemistry of Solid Surfaces, Department of Chemistry, College of Chemistry and Chemical Engineering, Xiamen University, 361005, Xiamen, China. E-mail: qfdong@xmu.edu.cn; mszheng@xmu.edu.cn; Fax: +86-0592-2183905; Tel: +86-0592-2185905

[b]Department of Chemistry, College of Chemistry and Life Science, Quanzhou Normal University, Quanzhou 362000, China

† Electronic supplementary information (ESI) available. See DOI: 10.1039/c4ta01493f

‡ These authors contribute equally to this work.

experimental conditions and precursors are highly desirable to achieve ultrahigh capacity and high-rate capability.

Along this direction, we synthesized three different SnO_2/rGO composites with different Sn precursors and selectively added the surfactant P123. When evaluated as anode materials for LIBs, one of the composites showed the best rate performance and excellent cyclic stability to the best of our knowledge. It is found that the tin precursor and surface properties of graphene are responsible for the good electrochemical performances.

2. Experimental

2.1 Preparation of GO

GO was synthesized from expanded graphite powder using a modified Hummers method. Specifically, 0.2 g expanded graphite powder, 0.2 g $NaNO_3$ and 1.2 g $KMnO_4$ were added into 24 mL concentrated sulphuric acid. After stirring overnight, the suspension was poured into 100 mL deionised water slowly with stirring. When the solution was cooled down to room temperature, 10 mL 30 wt% hydrogen peroxide (H_2O_2) was dropwise added into it. After stirring for 15 min, a luminous yellow GO suspension was obtained. The GO suspension was then centrifuged and washed with deionised water in turns several times, and finally the sol of GO was obtained.

2.2 Preparation of SnO_2/rGO composites

The as-prepared GO sol was diluted with 130 mL deionised water, and then 0.5 g P123 was added to it, resulting in a dark yellow solution after stirring. Then, 1.24 g stannous oxalate was added slowly into it. After stirring for 1 h, the mixture solution was heated to 180 °C for hydrothermal reactions for 2 h, resulting in a black suspension. The product was collected after a series of post-treatments, including suction filtration, washing with deionised water and absolute ethyl alcohol several times, and vacuum drying at 60 °C for 12 h. After grinding, the powders were further annealed at 300 °C for 5 h under N_2 flow to improve crystallinity. Finally, the SnO_2/rGO composite was obtained and denoted as composite **I**. The composite synthesized without adding P123 with the same procedure was named composite **II**; the composite prepared from $SnCl_4$ precursor following the composite **I** procedure was named composite **III**.

2.3 Characterizations

Thermogravimetric analysis was performed on Pyris Diamond TG-DTA (PE Co., US) in N_2/O_2 atmosphere to detect the contents of graphene in the composites. The samples were heated from 30 to 700 °C at a rate of 5 °C min^{-1}. The crystal structure of the samples was characterized using X-ray diffraction (XRD, Philips Panalytical X'pert), with Cu Kα radiation (λ = 1.54056 Å). Transmission electron microscopy (TEM, JEOL JEM-2100, 200 kV) and field-emission scanning electron microscopy (SEM Hitachi S-4800, 10 kV) were undertaken to characterize the structure and morphology of the composites. The X-ray photoelectron spectroscopy (XPS) measurement was performed using Quantum-2000 manufactured by PHI Corporation.

2.4 Electrochemical measurements

The electrochemical characteristics were analyzed with a half-cell configuration using CR2016 type coin cells by the galvanostatic charge–discharge technique. Li foil was used as the counter as well as reference electrode. SnO_2/rGO composites, Super-P and water soluble polymer *n*-lauryl acrylate (LA 5% Chengdu, China) with a mass ratio of 8 : 1 : 1 coated on a copper foil were directly used as the working electrode. The electrolyte was 1 M $LiPF_6$ in ethyl carbonate (EC)–dimethyl carbonate (DMC)–ethyl methyl carbonate (EMC) (volume ratio was 1 : 1 : 1). The voltage range was fixed from 0.02 to 3 V. Cyclic voltammetry (CV) measurements were conducted on a Princeton Applied Research Potentiostat model 263A at a scanning rate of 0.05 mV s^{-1}. Electrochemical impedance spectrometry (EIS) tests were done using IM6 (Zahner Elektrik) in a frequency range from 100 kHz to 100 MHz. Unless mentioned specifically, all the capacities in this article are based on the total mass of the SnO_2/rGO composites.

3. Results and discussion

We developed a convenient and environmentally friendly *in situ* method to produce SnO_2/rGO nanocomposites. Through the modified Hummers method, we obtained GO with abundant functional groups (*e.g.* carboxyl and hydroxyl), which promote the adsorption of Sn^{2+} ions on the surface of GO. Under hydrothermal conditions, Sn^{2+} ions were then hydrolyzed to SnO_2 nanoparticles, while GO was reduced to rGO synchronously. Since the oxygen containing groups serve as docks, SnO_2 nanoparticles were supposed to be uniformly dispersed on the surface of rGO. It is reported that chemical bonding between Sn element and carbon might exist in the composite.[40,41] The schematic diagram of the synthesis procedure for composite **I** is shown in Fig. 1. It should be pointed out that the random hybridization between SnO_2 nanoparticles and ultrathin rGO sheets can form 3-dimensional (3D) porous structure, which is beneficial for achieving high rate performance. The formed 3D electronic conduction network and reduced lithium ion diffusion length in SnO_2/graphene nanocomposite can facilitate transportation of electrons and lithium ions.

The morphology and structure of the three composites were thoroughly characterized by SEM and TEM. Fig. S1† shows the SEM images of composites **I**, **II** and **III**. Evidently, rGO showed a crumple morphology only in composite **I**, and was completely embedded in the other two samples. During the preparation of

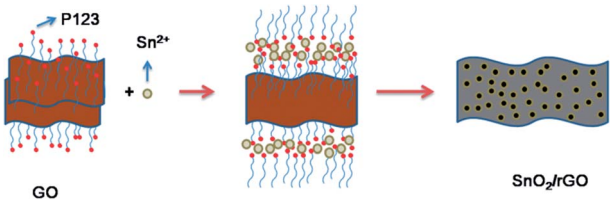

Fig. 1 Schematic illustration of the synthesis of SnO_2/rGO composites.

composite **I** and **III**, surfactant P123 was purposely added to suppress the aggregation of GO. However, the tin precursor of composite **III** was Sn^{4+}. This may be responsible for the disappearance of rGO for composite **III**. With regard to composite **II**, the absence of P123 might have a negative impact on the dispersion of rGO in the final product. Thus, both surfactant P123 and the tin precursors are crucial factors that influence the final morphologies of the composites. Detailed morphologies of the composites were characterized by TEM (Fig. 2). It is clearly observed that SnO_2 nanoparticles are uniformly dispersed on the layers of rGO for all the three samples (Fig. 2(a), (c) and (e)). After the ultrasonic treatment during the preparation of the TEM samples, the SnO_2 nanoparticles are still firmly adhered on the rGO surface. The distribution and size of SnO_2 particles prepared with Sn^{2+} precursors (composites **I** and **II**) on the rGO surface are marginally influenced by the use of P123. Composite **III** prepared with Sn^{4+} precursor exhibited a smaller SnO_2 particle size. Fig. 2(b), (d) and (f) show the crystal structure of the adsorbed nanoparticle, which can be assigned to SnO_2 with a (110) inter-planar spacing of 3.34 Å. This is consistent with the XRD result presented in Fig. 3(b). The sharp-edged shape and highly ordered crystalline structure of the SnO_2 particles can be ascribed to the high temperature annealing treatment. The insets of Fig. 2(b), (d) and (e) are the selected area electron diffraction (SAED) patterns of the composites, which suggest that the SnO_2 nanoparticles are polycrystalline. The spotty diffraction rings could be attributed to SnO_2 with cubic symmetry, while the diffuse contrast should be assigned to rGO.

The TG results of the three composites are shown in Fig. 3(a). It can be observed that additional weight loss takes place mainly between 300 and 700 °C for the SnO_2/rGO nanocomposites, which shows the contents of SnO_2 in the nanocomposites of **I**, **II**, and **III** as 82.7%, 78.8% and 82.7%, respectively, by assuming

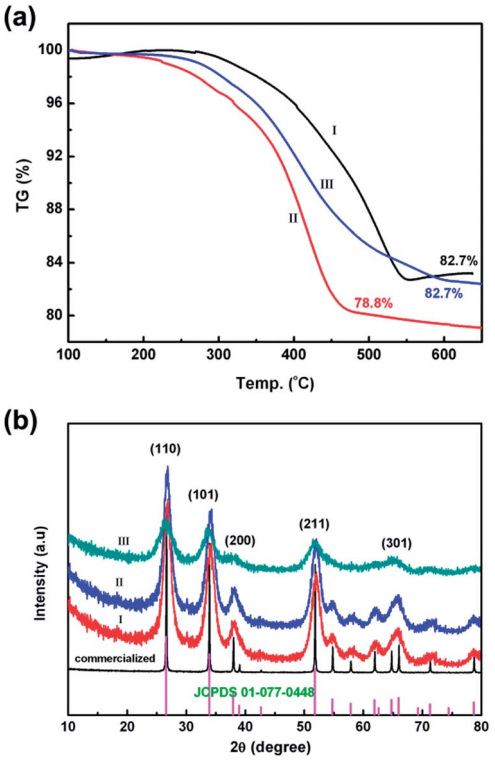

Fig. 3 TG curves (a) and XRD patterns (b) of I, II, and III.

that rGO has been completely burned off at this temperature range. It seems that the chemical compositions of the three composites are rather close, although the synthetic procedures were slightly different. The powder XRD patterns are displayed in Fig. 3(b). Compared with commercialized SnO_2, broadening in the peak full width at half maximum (FWHM) indicates that

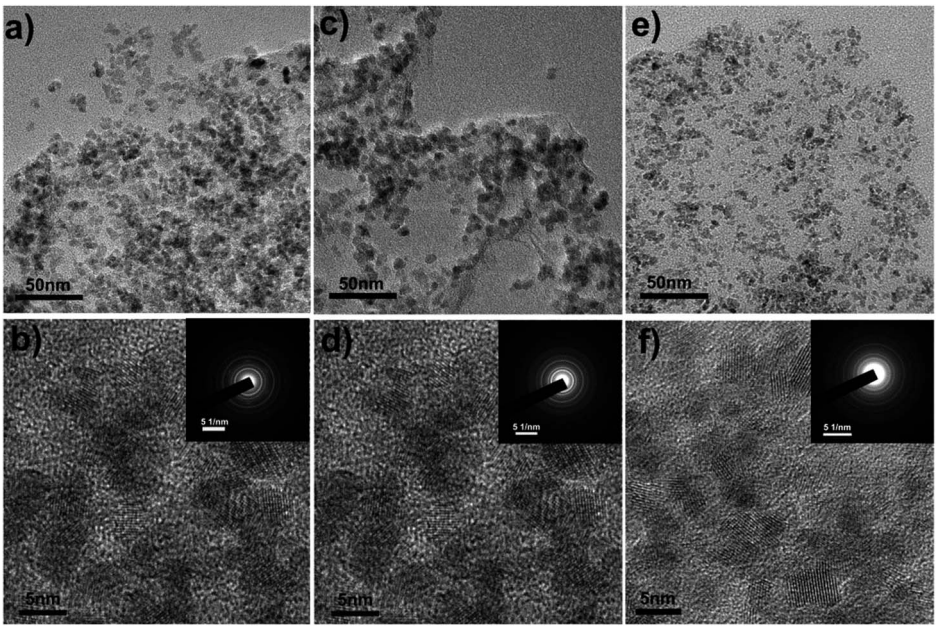

Fig. 2 TEM images and SAED patterns (inset) of composite I (a) and (b); composite II (c) and (d); composite III (e) and (f).

the sizes of the SnO_2/rGO composites are on the nanoscale. The crystallinity of SnO_2 nanoparticles is pronounced, as evident by the intensive diffraction peaks, especially the (110), (101), (200) and (211) peaks from tetragonal P42 (mnm) SnO_2 (JCPDS no. 01-077-0448). No other peaks are identified, indicating that the samples have good purity.

The N_2 adsorption–desorption isotherms and the pore size distribution of the three composites are shown in Fig. 4. The Brunauer–Emmett–Teller (BET) specific surface area of composite **I** is measured to be about 185 $m^2\ g^{-1}$. Nanocomposite electrode materials with large surface areas have led to multiple advances in the electrochemical performance of LIBs by providing shorter path lengths for lithium ion transports[42] and large electrolyte/active material contact area. The single point desorption total pore volume is 0.161 $cm^3\ g^{-1}$ and desorption average pore width is 3.48 nm for composite **I**. The data for the other two composites are also shown in Table 1. We found that sample **I** has the largest pore volume and relatively larger pore size. Compared to the other two composites, these properties can effectively maintain the nano-effect of the electrode and buffer the volume changes of the composite during the electrochemical reactions. This will benefit its structure stability during the lithiation and delithiation processes, thus improving the life time of the electrode.

In order to better understand the surface chemical compositions of the three composites, their XPS spectra have been recorded. The survey spectra are shown in Fig. 5(a). Only Sn, O and C elements are detected in the samples, indicating their high chemical purities. The binding energies of Sn 3d3/2 and Sn 3d5/2 are found to be 487.9 eV and 495.9 eV, respectively, which are the characteristics of SnO_2 compounds.[43] Broad C 1s core level emissions are obtained due to the existence of different carbon species,[44] which are presented in Fig. 5(b), (c) and (d) for composites **I**, **II** and **III**, respectively. The decomposed peaks centered at around 284.6, 285.8, 287 and 289.1 eV are attributed to C–C, C–O, C=O, and O–C=O, respectively.[45] The related

Table 1 The N_2 adsorption–desorption test results of the composites

Composite	Specific surface area ($m^2\ g^{-1}$)	Pore volume ($cm^3\ g^{-1}$)	Pore size (nm)
I	185	0.161	3.48
II	184.6	0.124	2.97
III	174.6	0.100	2.81

intensity of these bonds in different composites changes due to their different synthesis procedures. We calculated the intensity ratios of these bonds for different composites, which are shown in Table 2. Composite **I** has the highest content of C–C bonds and lowest content of C=O and O–C=O bonds, which suggest that the rGO in composite **I** has been well reduced. Composite **III** has the highest content of C–O bonds, implying that the GO in this composite was not well reduced. Normally, after hydrothermal treatment, the intensity ratio of O and C elements (I_O/I_C) decreases notably, as the large majority of the oxygenated species are removed from the graphene surface.[46] In composites **I** and **II**, by using the stannous oxalate precursor, Sn^{2+} ions can easily react with the oxygenated groups on the surface of GO, resulting in the removal of the oxygenated groups from its surface, leading to the increase of C–C bonds. In the case of composite **I**, with the help of surfactant P123, the surface O–C=O bonds can be further reduced. On the other hand, for composite **III**, Sn^{4+} ions are associated with the surface oxygenated groups of GO through electrostatic adsorption; the interaction is thus not strong enough to effectively remove the oxide groups from the GO surface, and consequently, composite **III** has the highest O/C ratio. This result indicates that a slight change in the synthesis conditions causes quite different interfacial interactions between SnO_2 and rGO. Particularly, the use of Sn^{2+} ions as the SnO_2 precursor removes more oxygen containing groups from the GO surface.

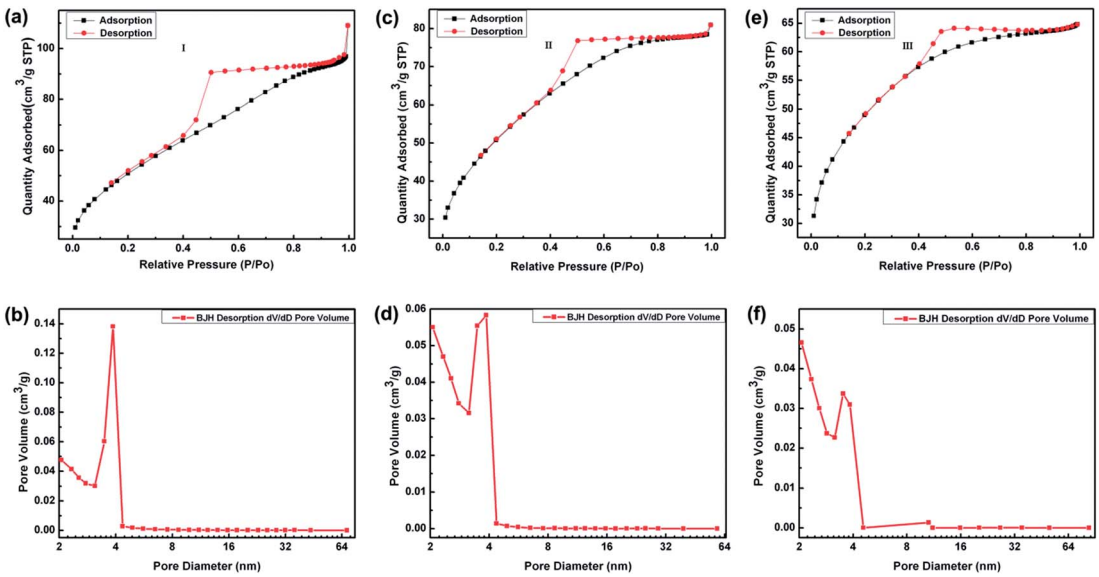

Fig. 4 N_2 adsorption–desorption isotherm loop and pore-size distribution plots of I (a) and (b); II (c) and (d) and III (e) and (f).

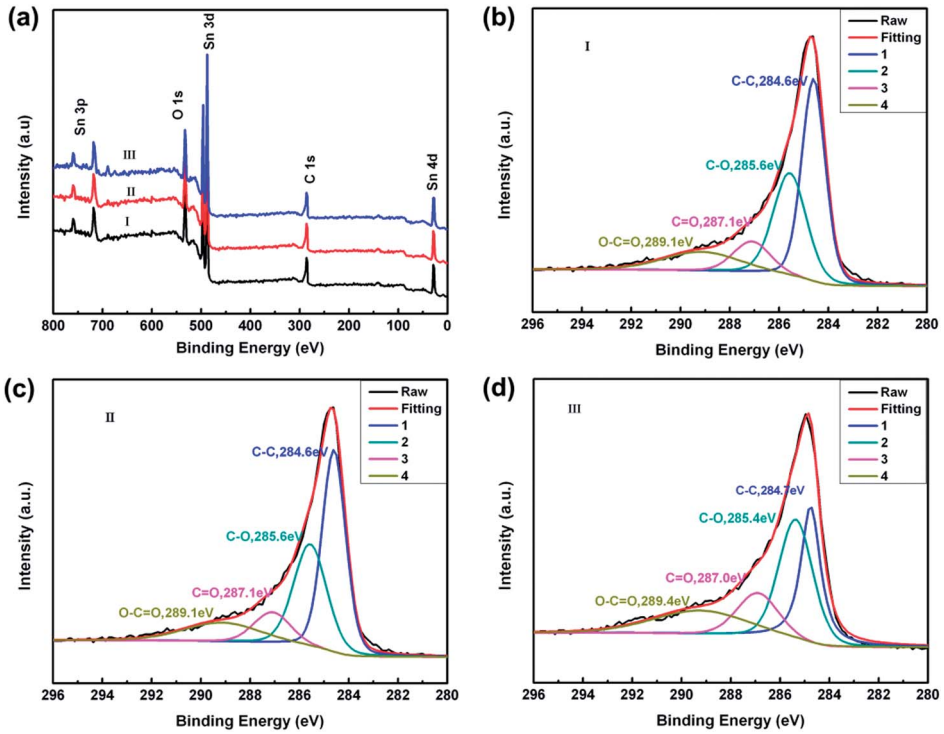

Fig. 5 (a) XPS survey spectra of the three composites. C 1s core level spectra of composites I (b), II (c) and III (d).

Table 2 Intensity ratios of C–C, C–O, C=O, and O–C=O for different composites

Composite	C–C (%)	C–O (%)	C=O (%)	O–C=O (%)
I	52.2	23.9	10.2	13.6
II	47.5	23.0	11.0	18.4
III	26.4	39.3	14.8	19.5

Galvanostatic charge–discharge and cyclic voltammetry (Fig. S2†) of the half-cells were performed between 0.02 and 3.0 V (*vs.* Li^+/Li). The composite **I** electrode delivers the highest rate capability, as shown in Fig. 6(a). When cycled at a high current density of 10 A g^{-1}, it still retains comparable capacities of over. 550 mA h g^{-1} and restores to a capacity of over 1024 mA h g^{-1} at 0.1 A g^{-1} again. SnO_2/graphene composites in previous studies could barely reach such a high current density with a reasonably high specific capacity (*e.g.* 580 mA h g^{-1} at 2 A g^{-1},[47] 203 mA h g^{-1} at 10 A g^{-1},[39] *etc.*) and exhibited rapid capacity fading.[48] To the best of our knowledge, this capacity at 10 A g^{-1} is the highest value reported in the literature. Though composites **II** and **III** also show competitive capacities of 1000 and 850 mA h g^{-1}, respectively, at low current rates (*e.g.* 0.1 A g^{-1}), they drop dramatically to 220 and 50 mA h g^{-1} when the current density increases to 10 A g^{-1}. The high capacities of the composites at low current density could be attributed to the nanosized SnO_2 and rGO matrix, which provides a large surface area and good mechanical properties.

The theoretical capacity values of SnO_2 at the first discharge could be calculated from $2Li_2O$ and $Li_{4.4}Sn$ with the capacity of 1494 mA h g^{-1}. If we assume that the capacity of rGO is 372 mA h g^{-1},[49,50] the theoretical discharge capacity of the three composites (80% SnO_2 plus 20% graphene) is about 1274 mA h g^{-1} for the first cycle. In Fig. 6(b), in the initial 5 cycles, the electrodes are first activated at a low current density of 0.1 A g^{-1}, then undergo next 5 cycles at 0.2 A g^{-1}, followed by the required current density of 0.5 A g^{-1}. The discharge capacities for the composites at the 1st, 11th, and 200th cycles are listed in Table 3. Composites **I**, **II**, and **III** have a similar first discharge capacity of about 1930 mA h g^{-1}, which is higher than the theoretical value (1274 mA h g^{-1}). This can be attributed to the formation of solid electrolyte interface (SEI) layers on the electrodes' surfaces and the consumption of Li^+ by the defects on the rGO surface. At the 11^{th} cycle, their capacities drop to 1160, 1069, and 625 mA h g^{-1}, and after 200 cycles, they are 951, 810, and 171 mA h g^{-1}, respectively. It is obvious that composite **I** exhibits the highest capacity and best capacity retention, which is 82.0% by comparing its stable capacity at the 11^{th} and 200^{th} cycles. The cyclic performance of composite **I** at different current densities is shown in Fig. 6(c). The same conclusion as obtained from Fig. 6(a) can be drawn that the capacities at current densities of 0.2 A g^{-1} and 2 A g^{-1} are not quite different, which are 904 and 739 mA h g^{-1}, respectively, after 200 cycles. Composite **I** retains 90.8%, 76.8%, and 62.3% of the discharge capacity after 200 cycles in comparison with that at the 11^{th} cycle at the current densities of 0.2, 1 and 2 A g^{-1}, respectively. Fig. 6(d) shows the charge–discharge profiles of composite **I** at the 1^{st}, 10^{th}, 50^{th}, 100^{th}, and 200^{th} cycles with a current density of 0.5 A g^{-1}. In general, the SnO_2-based anode shows classical plateaus around 0.8 V, which has been well known to be due to formation of the

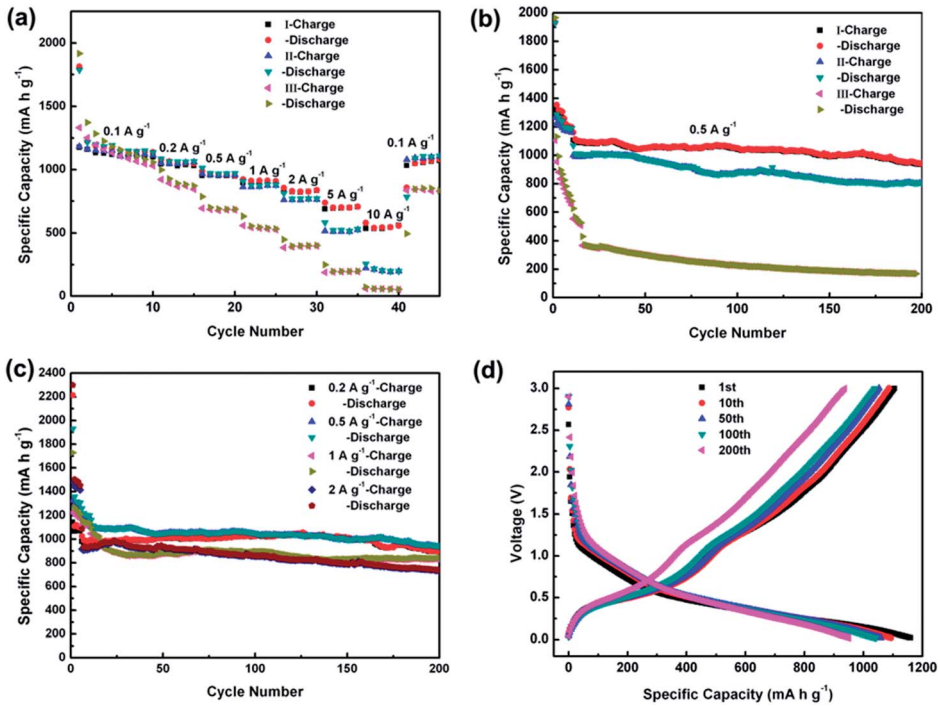

Fig. 6 (a) Rate performances of the three composites, (b) cycle performances of the three composites at the current density of 0.5 A g^{-1}, (c) cycle performances of composite I at different current densities, (d) charging–discharging curves of composite I at the rate of 0.5 A g^{-1}.

Table 3 Discharge capacities (mA h g^{-1}) of the three composites at different cycle numbers (current density: 0.5 A g^{-1})

Composite	1^{st}	11^{th}	200^{th}
I	1931	1160	951
II	1929	1069	810
III	1965	625	171

SEI layers. However, in our study, this plateau is not significant, which indicates that only a small number of SEI layers are formed at the electrode surface. Such a result is related to the enhanced surface electrochemical reactivity. The shape of the profiles did not change significantly during cycling, indicating the good stability of composite **I**.

The outstanding electrochemical performance can be mainly ascribed to three factors. First, the particles of SnO_2 in composite **I** are minimized to a size of about 5 nm with a large surface area and proper pore size. It would enhance the structural stability in insertion and desertion processes of Li ions when cycling. Second, well reduced GO as a good matrix not only enhances the conductivity but also reduces the aggregation of SnO_2. Further, rGO could also provide a large contact surface area and volume expansion space for SnO_2 particles. The perfection of C–C bond in rGO is a key factor to the good electrochemical performance for LIBs. Third, SnO_2 are uniformly dispersed on rGO to form homogeneous electro-active composites in the electrode film without any aggregation. Compared to Sn^{4+}, Sn^{2+} ions can react with oxygen containing groups of GO and result in better reduced rGO, and possibly form C–Sn–O bonds. These features guarantee a rapid transport of interfacial electrons/lithium ions and high-rate performances.

AC impedance spectra (Fig. 7) were obtained for the three composite electrodes to understand the origin of their electrochemical performance differences. The electrochemical impedance measurements were performed after the cells were cycled for 100 cycles. All the impedance responses show a semicircular loop at higher frequencies and straight line at lower frequencies. The intercept on the Z' real axis in the high frequency region is ascribed to the resistance of the electrolyte. The middle semicircle corresponds to the charge transfer resistance (R_{ct}) at the electrode/electrolyte interface. The inclined line in the low frequency range indicates the Warburg

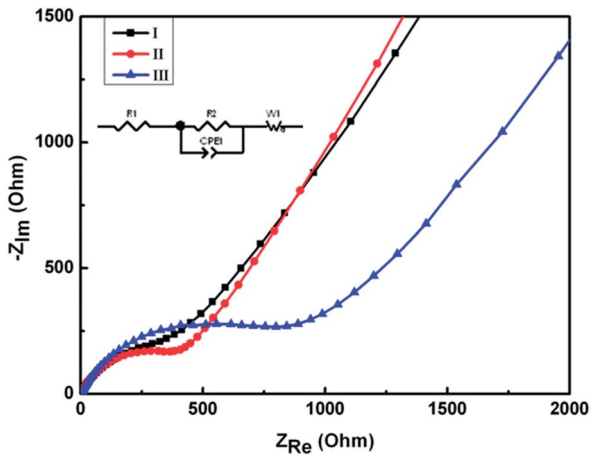

Fig. 7 AC impedance spectra of the three composite electrodes.

impedance, relating to the solid-state diffusion of lithium ions in the electrode materials.[51] In Fig. 7, the difference in R_{ct} of the three electrodes is obvious, with R_{ct} values of 340 Ω, 372 Ω, and 788 Ω for composites **I**, **II**, and **III**, respectively. Considering that the diameter of Cu foils is the same, the amount of active materials is the main factor that influences the EIS behaviors of the electrodes. After normalized to the mass values, the corresponding R_{ct} values for composite **I**, **II** and **III** are 315, 369 and 1082, respectively. The small R_{ct} value explains the good electrochemical reaction properties of the composite **I** electrode, which means that it has the lowest electrode/electrolyte interfacial resistance and the fastest solid-state diffusion rate of Li ions inside the electrode.

4. Conclusions

We reported a convenient and environmentally friendly *in situ* method to synthesize SnO_2/rGO composites. Experimental results indicated that the excellent electrochemical performances can be attributed to the surface status of the composites rather than the particle size and morphology. XPS results showed that the SnO_2/rGO composite with Sn^{2+} precursor source and the assistance of P123 has more C–C bonds. Electrochemical measurements demonstrated that the well reduced rGO in the composite strongly influences the interfacial interaction between SnO_2 nanoparticles and rGO matrix. Composite **I** exhibited excellent cycle and rate performances, showing a high Li^+ storage capacity of 550 mA h g^{-1} even at a current density of 10 A g^{-1} and good capacity retention of 82.0% at a scan rate of 2 A g^{-1} after 200 cycles. Our work introduced a new guideline in synthesizing transition metal oxide/rGO composites with high and stable electrochemical performance for LIBs, and a new horizon for the design and control of interface properties of composite materials.

Acknowledgements

We gratefully acknowledge the financial support from the Key Project of NSFC (U1305246, 21321062) and the Major Project funded by Xiamen city (3502Z20121002). Wu would like to thank Quanzhou "Tong-Jiang Scholar" program, Fujian "Min-Jiang Scholar" program, program for New Century Excellent Talents in University (NCET-13-0879), the Education and Scientific Research Foundation (Class A) for Young Teachers of Education Bureau of Fujian Province, China (Grant no. JA13263), and National Natural Science Foundation of China (Grant no. 21353001) for financial support.

References

1 M. Armand and J. M. Tarascon, *Nature*, 2008, **451**, 652–657.
2 J. B. Goodenough and Y. Kim, *Chem. Mater.*, 2010, **22**, 587–603.
3 J. M. Tarascon and M. Armand, *Nature*, 2001, **414**, 359–367.
4 Y. P. Wu, E. Rahm and R. Holze, *J. Power Sources*, 2003, **114**, 228–236.
5 H. Buqa, D. Goers, M. Holzapfel, M. E. Spahr and P. Novak, *J. Electrochem. Soc.*, 2005, **152**, A474–A481.
6 Y. Idota, M. Nishima, Y. Miyaki and T. Kubota, Eur. Pat., 0651450A1, 1995.
7 X. W. Lou, C. M. Li and L. A. Archer, *Adv. Mater.*, 2009, **21**, 2536–2539.
8 Z. Chen, M. Zhou, Y. Cao, X. Ai, H. Yang and J. Liu, *Adv. Energy Mater.*, 2012, **2**, 95–102.
9 Y. Wang, J. Y. Lee and H. C. Zeng, *Chem. Mater.*, 2005, **17**, 3899–3903.
10 D. Larcher, S. Beattie, M. Morcrette, K. Edstroem, J. C. Jumas and J. M. Tarascon, *J. Mater. Chem.*, 2007, **17**, 3759–3772.
11 D. Deng and J. Y. Lee, *Chem. Mater.*, 2008, **20**, 1841–1846.
12 N. Zhao, G. Wang, Y. Huang, B. Wang, B. Yao and Y. Wu, *Chem. Mater.*, 2008, **20**, 2612–2614.
13 M. S. Park, G. X. Wang, Y. M. Kang, D. Wexler, S. X. Dou and H. K. Liu, *Angew. Chem., Int. Ed.*, 2007, **46**, 750–753.
14 C. Wang, Y. Zhou, M. Y. Ge, X. B. Xu, Z. L. Zhang and J. Z. Jiang, *J. Am. Chem. Soc.*, 2010, **132**, 46–47.
15 N. Du, H. Zhang, J. Chen, J. Sun, B. Chen and D. Yang, *J. Phys. Chem. B*, 2008, **112**, 14836–14842.
16 Z. Y. Wang, D. Y. Luan, F. Y. C. Boey and X. W. Lou, *J. Am. Chem. Soc.*, 2011, **133**, 4738–4741.
17 J. Fan, T. Wang, C. Z. Yu, B. Tu, Z. Y. Jiang and D. Y. Zhao, *Adv. Mater.*, 2004, **16**, 1432–1436.
18 X. W. Lou, J. S. Chen, P. Chen and L. A. Archer, *Chem. Mater.*, 2009, **21**, 2868–2874.
19 F. M. Courtel, E. A. Baranova, Y. Abu-Lebdeh and I. J. Davidson, *J. Power Sources*, 2010, **195**, 2355–2361.
20 Z. H. Wen, Q. Wang, Q. Zhang and J. H. Li, *Adv. Funct. Mater.*, 2007, **17**, 2772–2778.
21 Z. Y. Wang, G. Chen and D. G. Xia, *J. Power Sources*, 2008, **184**, 432–436.
22 Q.-G. Shao, W.-M. Chen, Z.-H. Wang, L. Qie, L.-X. Yuan, W.-X. Zhang, X.-L. Hu and Y.-H. Huang, *Electrochem. Commun.*, 2011, **13**, 1431–1434.
23 H. X. Zhang, C. Feng, Y. C. Zhai, K. L. Jiang, Q. Q. Li and S. S. Fan, *Adv. Mater.*, 2009, **21**, 2299–2304.
24 C. Rao, A. Sood, K. Subrahmanyam and A. Govindaraj, *Angew. Chem., Int. Ed.*, 2009, **48**, 7752–7777.
25 S. M. Paek, E. Yoo and I. Honma, *Nano Lett.*, 2009, **9**, 72–75.
26 D. H. Wang, R. Kou, D. Choi, Z. G. Yang, Z. M. Nie, J. Li, L. V. Saraf, D. H. Hu, J. G. Zhang, G. L. Graff, J. Liu, M. A. Pope and I. A. Aksay, *ACS Nano*, 2010, **4**, 1587–1595.
27 X. J. Zhu, Y. W. Zhu, S. Murali, M. D. Stoller and R. S. Ruoff, *J. Power Sources*, 2011, **196**, 6473–6477.
28 H. Kim, S. W. Kim, Y. U. Park, H. Gwon, D. H. Seo, Y. Kim and K. Kang, *Nano Res.*, 2010, **3**, 813–821.
29 J. G. Ren, C. Wang, Q. H. Wu, X. Liu, L. He and W. Zhang, *Nanoscale*, 2014, **6**, 3353–3360.
30 C. Wang, Y. Li, Y. S. Chui, Q. H. Wu, X. Chen and W. Zhang, *Nanoscale*, 2013, **5**, 10599–10604.
31 G. Hong, Q. H. Wu, J. Ren, C. Wang, W. Zhang and S. T. Lee, *Nano Today*, 2013, **8**, 388–402.
32 Q. H. Wu, *Crit. Rev. Solid State Mater. Sci.*, 2013, **38**, 318–352.
33 J. G. Ren, Q. H. Wu, H. Tang, G. Hong, W. J. Zhang and S.-T. Lee, *J. Mater. Chem. A*, 2013, **1**, 1821–1826.

34 Z. S. Wu, W. C. Ren, L. Wen, L. B. Gao, J. P. Zhao, Z. P. Chen, G. M. Zhou, F. Li and H. M. Cheng, *ACS Nano*, 2010, **4**, 3187–3194.
35 H. L. Wang, L. F. Cui, Y. Yang, H. S. Casalongue, J. T. Robinson, Y. Y. Liang, Y. Cui and H. J. Dai, *J. Am. Chem. Soc.*, 2010, **132**, 13978–13980.
36 G. M. Zhou, D. W. Wang, F. Li, L. L. Zhang, N. Li, Z. S. Wu, L. Wen, G. Q. Lu and H. M. Cheng, *Chem. Mater.*, 2010, **22**, 5306–5313.
37 P. C. Lian, X. F. Zhu, S. Z. Liang, Z. Li, W. S. Yang and H. H. Wang, *Electrochim. Acta*, 2011, **56**, 4532–4539.
38 S. Ding, D. Luan, F. Y. Boey, J. S. Chen and X. W. Lou, *Chem. Commun.*, 2011, **47**, 7155–7157.
39 X. S. Zhou, Y. X. Yin, L. J. Wan and Y. G. Guo, *J. Mater. Chem.*, 2012, **22**, 17456–17459.
40 D. N. Wang, J. L. Yang, X. F. Li, D. S. Geng, R. Y. Li, M. Cai, T. K. Sham and X. L. Sun, *Energy Environ. Sci.*, 2013, **6**, 2900–2906.
41 X. S. Zhou, L. J. Wan and Y. G. Guo, *Adv. Mater.*, 2013, **25**, 2152–2157.
42 A. S. Aricò, P. Bruce, B. Scrosati, J. M. Tarascon and W. van Schalkwijk, *Nat. Mater.*, 2005, **4**, 366–377.
43 C. H. Xu, J. Sun and L. Gao, *Nanoscale*, 2012, **4**, 5425–5430.
44 K. Haubner, J. Murawski, P. Olk, L. M. Eng, C. Ziegler, B. Adolphi and E. Jaehne, *ChemPhysChem*, 2010, **11**, 2131–2139.
45 S. Stankovich, D. A. Dikin, R. D. Piner, K. A. Kohlhaas, Y. Y. Jia, Y. Wu, S. T. Nguyen and R. S. Ruoff, *Carbon*, 2007, **45**, 1558–1565.
46 C. H. Xu, J. Sun and L. Gao, *J. Mater. Chem.*, 2012, **22**, 975–979.
47 J. Lin, Z. Peng, C. Xiang, G. Ruan, Z. Yan, D. Natelson and J. M. Tour, *ACS Nano*, 2013, **7**, 6001–6006.
48 J. Li, W. Wan, H. Zhou, J. Li and D. Xu, *Chem. Commun.*, 2011, **47**, 3439–3441.
49 S. M. Paek, E. J. Yoo and I. Honma, *Nano Lett.*, 2009, **9**, 72–75.
50 X. Y. Wang, X. F. Zhou, K. Yao, J. G. Zhang and Z. P. Liu, *Carbon*, 2011, **49**, 133–139.
51 B. Wang, D. W. Su, J. Park, H. Ahn and G. X. Wang, *Nanoscale Res. Lett.*, 2012, **7**, 215–221.

